A integrated framework for surface deformation modeling and induced seismicity forecasting due to reservoir operations

Hadrien Meyer *, Jonathan D. Smith *, Stephen Bourne †, Jean-Philippe Avouac *‡

May 2022

Abstract

Induced seismicity and surface deformation are common observable manifestations of the geomechanical effect of reservoir operations whether related to geothermal energy production, gas extraction, or the storage of carbon dioxyde, gas, air or hydrogen. Modeling tools to predict quantitatively surface deformation and seismicity based on operation data could thus help manage such reservoirs. To that effect, we present an integrated modeling framework which combines reservoir modeling, geomechanical modeling and earthquake forecasting. To allow effective computational cost, we assume vertical flow equilibrium, semi-analytical Green functions to calculate surface deformation and poro-elastic stresses, and a simple earthquake nucleation model based on coulomb stress changes. We use the test case of the Groningen gas field in the Netherlands to validate the modeling framework and demonstrate its usefulness for reservoir management.

1 Introduction

The demand for increasing clean energy is driving various industry operations that involve either injecting or extracting fluids from the sub-surface. These operations include the storage of carbon dioxyde, air, gas or hydrogen, gas extraction or geothermal energy production. They imply pressure changes and geomechanical deformation which can lead to measurable surface displacements and seismicity (Vasco et al. [2018], Rutqvist et al. [2016]).

Seismicity is a concern, because of the hazard paused to infrastructures and residents, but also because it could jeopardize the mechanical integrity of a reservoir in case of fracturing of the caprock. Surface deformation isn't a major liability but can be a valuable source of information pressure changes in the reservoir. For these reasons there would be most value in computationally effective methods to relate reservoir operations (well flow rates and pressures) to surface deformation and seismicity. We present here such a framework. We use the well documented example of the Groningen gas field in the Netherlands (Figure 1), where gas extraction has caused measurable subsidence since the 1960s and induced seismicity since the 1990s due to the gas extraction (Bourne et al. [2014]) prompting large efforts to monitor the seismicity and surface deformation and public release of information on the reservoir characteristics. There is therefore a wealth of information publicly

*Geology and Planetary Science Division, California Institute of Technology, Pasadena, CA, USA
†Shell Global Solutions, Amsterdam, Netherlands
‡Corresponding author(avouac@caltech.edu)

available on this reservoir (de Jager and Visser [2017], Burkitov et al. [2016], Dost et al. [2017]) and it has therefore been used as a test case in a number of previous studies of surface subsidence and induced seismicity (Bourne et al. [2014], Bourne and Oates [2017], Bourne et al. [2018], Buijze et al. [2017], Smith et al. [2019], Buijze et al. [2019], Candela et al. [2019], Dempsey and Suckale [2017], van Wees et al. [2019], Heimisson et al. [2021], Richter et al. [2020]). The region has experienced induced seismicity with small magnitudes starting in the 1990s (Figure 1b). Stronger and more frequent seismic events in 2012 caused public alarm and led authorities to request a reduction of production and complete shut down by 2030. Production went from 53.8 billions bcm in 2012 to about 20 bcm in 2018 and is supposed to decrease down to 12 bcm per year in 2018-2023 and completely cease by 2030 (Figure 1c).

This paper describes a modeling workflow which includes a simplified reservoir model based on the Vertical Flow Equilibrium (VFE) approximation, a Green's function approach to calculate poroelastic stress changes and surface subsidence, and a simple earthquake nucleation model to relate stress changes to seismicity. We demonstrate the performance of this workflow and shows that it can be used to test production scenario and eventually help design pressure management so as to minimize geomechanical effects and induced seismicity. We use our workflow to forecast the geomechanical effects and induced seismicity, with account for uncertainties on the model parameters, based on the 'cold winter' production scenario (Nederlandse Aardolie Maatschappij [2013]) from the end of 2016 to 2030, a shut-in scenario with arrest of the production at the end of 2016 and, as a thought experiment, a cold winter scenario with pressure management.

2 Setting of the Groningen Gas Field

The Groningen gas field was discovered in 1959 and has been in production since 1962 (Bourne et al. [2014]). It extends approximately by 35 km East-West and 50 km North-South. The reservoir is located in the Upper Permian Rotlingend formation, a sequence of fluvial-aeolian sandstones-conglomerates-clay. It was deposited in the Permian in a rift basin with a South-West to North-East distal to proximal facies trend from conglomerate-rich in the South, to sandstones-rich in the center of the Reservoir and clay-rich in the North (Stauble and Milius [1970], de Jager and Visser [2017]). The reservoir lies a depth of about 3000m and dips by about 3 degrees northwards, corresponding to $\approx$ 600m deepening over its 40km extent. Its thickness increases from 90m in the South-East to 300m in the North West. An overlying thick and impermeable layer of evaporite and anhydrite provide the seal for the reservoir. This caprock formation comprises a 50-m-thick basal anhydrite and 0.2- to 1-km-thick evaporite with disconnected anhydrite lenses. The reservoir is structurally controlled by normal faults in the East, South and West and closed by an aquifer in the North (de Jager and Visser [2017]).

The initial gas reserve was estimated to 2,9139 bcm (Burkitov et al. [2016]) and about 2,200 bcm had been produced as of May 2017. The reservoir is layered (Burkitov et al. [2016]) with the free gas layer on top of the water interface. Due to the northern dip of the reservoir, the water-gas contact is responsible of the North boundary (Burkitov et al. [2016]). Because of its limited connection to groundwater, gas extraction has led to a significant pressure drop driven gas expansion and pressure drop. This is concordant with the pressure depletion through time and the small amount of water extracted (Burkitov et al. [2016]).

The reservoir has a permeability ranging from tens of milli-Darcy ($1mD = 9.869233 \times 10^{-16} m^{-2}$) up to a few Darcy with an average value of 260 milli-Darcy ($3.55 \times 10^{-13} m^{-2}$), with higher values in the center of the reservoir (Burkitov et al. [2016]). The porosity range from 10% to 25% with a mean value of 17% and a similar spatial distribution with larger values near the center of the reservoir (Burkitov et al. [2016]). The initial pressure of the reservoir was about 34.68 MPa, close to hydrostatic as expected (Burkitov et al. [2016]). The geothermal gradient is estimated to 27K/km leading so that the reservoir temperature ranges from 80 °C to 120 °C with a mean value of 102 °C. The gas is composed of 14% of Nitrogen, 1% of Carbon Dioxide (CO_2) and the rest is mainly methane (CH_4) (Stauble and Milius [1970], Burkitov et al. [2016]) and therefore can be described as a dry gas (Yang [2016]) and was modeled that way in the GFR2012 but has been updated and is modeled as a wet gas in GFR2015 because of the condensed water dissolved in the gas (Burkitov et al. [2016]).

3 Reservoir Modeling

State-of-the-art reservoir models can account for two-way interaction between a reservoir model and geomechanics model through macroscopic theory of poroelasticity (Jha and Juanes [2014]). These fully coupled reservoir models have been used to investigate our mechanistic understanding of induced seismicity (Juanes et al. [2016], Byrne et al. [2020], Kroll et al. [2020]). However, they also require substantial computational cost and thus makes it challenging to perform the large number of realizations needed to match observstions or to make data-driven predictions with account for uncertainties. To circumvent the heavy computational cost of a full 3D reservoir geomechanics model, recent studies have made simplifications of the model physics and/or reductions in physical dimensions. Analytical solutions of linear poroelasticity (Wang [2018]) can be used to predict surface deformation and induced seismicity in ideal cases of diffusion in 2-D or 3-D in a unbounde medium (Zhai and Shirzaei [2018], Zhai et al. [2019]). The approach, however, is limited to single-phase flow and is not suited to model fluid flow within a reservoir of finite dimension with complex geometry. Reduction in model dimension is another strategy that we adopt in this study. In the sub-sections below we first describe briefly the industry reservoir model which we used to benchmark our model and then provide details on our implementation of the VFE model and history matching.

3.1 Industry High-Resolution Pressure Depletion Model

The current standard used to model pressure depletion within the reservoir is MoReS (Modular Reservoir Simulator) which is used for business purposes and risk assesment (Nederlandse Aardolie Maatschappij [2013]). It accounts for the detailed reservoir geometry which was determines based in seismic reflection and seismic refraction data (Burkitov et al. [2016]): shape, faults, thickness and depth. The model ignores poro-elastic coupling but can be used to predict poroleastic deformation. The water-gas interaction is represented using a Pressure-Volume-Temperature (PVT) two-phase fluid flow model. The model depends on 96 adjustable parameters, These parameters were optimized through history matching using the production data (wells flow rates) and the borehole pressure measurements (Nederlandse Aardolie Maatschappij [2013]). However, this procedure is computationally expensive requiring hundreds of computational hours to compute a single history matched model, only returning the optimal solution without quantification of uncertainties. We use MoReS to benchmark our simplified reservoir model.

3.2 Simplifying assumptions

We aim at a computationally efficient reservoir model that can be used to forecast seismicity, with quantification of the uncertainties resulting from matching both the reservoir data and the seismicity observations. This objective requires a computationally effective workflow as the models are not linear and parameter estimation requires resorting to non-linear methods such as the Monte-Carlo Markov-Chain algorithm. Regarding the reservoir model, we make two major simplifications. We assume Vertical Flow Equilibrium, which leads to a 2-D instead of a 3-D calculation (Coats et al. [1971]).

The reservoir is considered planar with a spatial extent identical to that used in MoReS and which (Burkitov et al. [2016]) which is clearly consistent with the pattern of surface subsidence (Smith et al. [2019])(Figure 1a). We assume no flow at the boundaries, which is probably realistic for the eastern, western and southern boundaries which are fault bounded. This condition is more questionable for the northern boundary which is bounded by an aquifer. The reservoir is additionally supposed to be horizontal, which is reasonable given the overall dip of the reservoir caprock. the reservoir is assumed entirely connected. Some areas near the southern and western edges of the reservoir have a pressure history than could suggest poor hydraulic connection with the main part of the reservoir (Burkitov et al. [2016]).

We simulate pressure diffusion in the reservoir assuming Vertical Flow Equilibrium (Coats et al. [1971]). This assumption leads to approximate pressure diffusion in 3-D with a 2-D calculation whereby only the vertically-integrated pressure and flow are solved for. This method has been used to model pore-pressure diffusion or gravity driven flow of CO2 (Cowton et al. [2018]) and can be extended to model multiphase flow (Jenkins et al. [2019]). The VFE is valid if the ratio of the horizontal diffusion time over the vertical diffusion time is typically larger than 10 (Yortsos [1991]). This ratio expressed as a function of the thickness, Δz, the horizontal extent, Δx, and the vertical and horizontal permeabilities, k_z and k_x, writes:

$$R_L = \left(\frac{\Delta x}{\Delta z}\right) \cdot \left(\frac{k_z}{k_x}\right)^{\frac{1}{2}} \tag{1}$$

In the Groningen reservoir case, permeability can be assumed isotropic due to the conglomeratic and sandstone lithology. With $k_z = k_x$, Δz of up 300 meters, and Δx between 35 and 50 kilometers we find $R_L > 117$, so the condition for the validity of the VFE approximation is met.

Finally, we assume that the gas fills the entire thickness of the reservoir while the height of the gas layer might in fact occupy only a fraction of it. We therefore add a parameter, the gas saturation, to account for this. As a result our model depends only on 3 parameters: permeability, porosity and gas saturation. They are assumed uniform in space and constant in time. Not that we neglect the effect of sediment facies variation in space and of reservoir compaction on temporal variations of porosity and permeability. We also neglect that the gas saturation could be changing due to possible aquifer intrusion into the depleting reservoir. The 3 unknowns are solved for through history matching.

3.3 Governing equations

The governing equations are derived from mass conservation and the balance of linear momentum for fluid flow in a porous medium (De Marsily [1986]). The mass conservation equation writes:

$$\frac{(\partial \phi \rho)}{\partial t} + \nabla(\rho u) = q. \tag{2}$$

where ϕ is the porosity (comprised between 0 and 1), ρ is the density of the fluid, u is the fluid velocity and q is the source term representing injection or extraction of fluid. Darcy's Law (Darcy [1856]) writes:

$$u = \left(\frac{-k}{\mu} \nabla p + \rho g z \right), \tag{3}$$

where μ is the fluid dynamic viscosity and p the pressure. Combining (2) and (3) and ignoring the gravity effect thanks to the Vertical Flow Equilibrium assumption, (Coats et al. [1971]) yields :

$$\frac{(\partial \phi \rho)}{\partial t} + \nabla \cdot \left[\rho \left(\frac{-k}{\mu} \nabla p \right) \right] = q. \tag{4}$$

The development of (4) relating each term to the pressure gives:

$$\phi \frac{d\rho}{dp} \frac{dp}{dt} + \rho \frac{d\phi}{dp} \frac{dp}{dt} + \nabla \cdot \left(-\rho \frac{k}{\mu} \nabla p \right) = q. \tag{5}$$

Assuming that the compressibility of the solid grains is at least one order of magnitude lower than the compressibility of the bulk matrix ($\beta_s << \beta_m$) and that the regional stress has been constant (Birdsell et al. [2018]) during the exploitation of the reservoir we get :

$$\beta_m = \frac{-1}{V_{tot}} \frac{dV_{tot}}{d\sigma'} = \frac{1}{1-\phi} \frac{d\phi}{dp}. \tag{6}$$

We can now write (5) using (6):

$$\phi \frac{d\rho}{dp} \frac{dp}{dt} + (1-\phi)\rho\beta_m \frac{dp}{dt} + \nabla \cdot \left(-\rho \frac{k}{\mu} \nabla p \right) = q. \tag{7}$$

The matrix compressibility for the Groningen reservoir is estimated to $\beta_m \approx 1 - 10 \times 10^{-11} Pa^{-1}$ (Burkitov et al. [2016], van Eijs and van der Wal [2017]). The fluid density is given by the equation of state (Yang [2016]) :

$$\rho = \frac{PM}{ZRT}, \tag{8}$$

where P is pressure, M is molar weight of the gas, R is the Gas constant, T is temperature and Z is compressibility factor, comprised between 0 and 1. The compressibility factor also depends on the temperature, pressure and composition, and can either be calculated using polynomial function or extracted from charts. The Groningen Gas is composed of mainly methane (CH_4) (85%), Nitrogen (N) (14%) and carbon dioxide (CO_2) (1%). The molar weight used in this study is the mean value over the 6 PVT zones considered in MoReS (Burkitov et al. [2016]) $M = 18.3815 g \cdot mol^{-1}$. For methane at a temperature of 385K and pressure between 5 and 40 MPa, Z-factor varies between 0.95

and 1.02. For simplicity it is assumed to be constant and equal to 1. The term $\frac{d\rho}{dp}$ on the left-hand side of the equation is then a constant:

$$\frac{d\rho}{dp} = \frac{M}{ZRT}. \tag{9}$$

A comparison of the time dependent terms indicates that the second term of the left-hand side $(1-\phi)\rho\beta_m\frac{dp}{dt}$ can be neglected because of the compressibility term, which is extremely low and therefore $(1-\phi)\rho\beta_m\frac{dp}{dt} \approx 8 \cdot 10^{-9} << \phi\frac{d\rho}{dp}\frac{dp}{dt} \approx 9 \cdot 10^{-7}$. This mean 7 can be simplified to :

$$\phi\frac{d\rho}{dp}\frac{dp}{dt} + \nabla \cdot \left(-\rho\frac{k}{\mu}\nabla p\right) = q. \tag{10}$$

The source term, representing the flow rates at he wells, is given in $kg \cdot m^{-3} \cdot s^{-1}$. It is converted to a two-dimension source term in $kg \cdot m^{-2} \cdot s^{-1}$ by dividing by the local thickness of the reservoir, Δz :

$$q = \frac{Q}{\Delta z}, \tag{11}$$

where Q is the source term in $kg \cdot m^{-3} \cdot s^{-1}$ and correspond to the extracted flux. The wells being considered as point sources, the area is taken to be 1 square meter. This assumption means there is an equal extraction along the thickness of the reservoir, an assumption consistent with the Vertical Flow Equilibrium hypothesis. Taking the gas saturation into account, the differential equation governing pressure diffusion with the VFE assumption is reduced to:

$$\phi\frac{d\rho}{dp}\frac{dp(x,y,t)}{dt} - \nabla \cdot \left(\rho(x,y,t)\frac{k}{\mu(x,y,t)}\nabla p(x,y,t)\right) = \frac{Q(x,y,t)}{\Delta z(x,y) * GasSaturation}, \tag{12}$$

where $\nabla = \frac{\partial}{\partial x} + \frac{\partial}{\partial y}$.

The equation is then solved using the open-source finite element solver FEniCS (Alnaes et al. [2015]) with an implicit Euler method for time discretization, using a time step of one month. The source terms are then monthly average extraction rates. The equation solves for the pressure at each time step given the extraction history. The viscosity and density are computed using the formulation given by (Yang [2016]): see 8 and $\mu = 10^{-4}Kexp(X\rho_g^y)$ that is the empirical formula of Lee-Gonzalez (Lee et al. [1966]) and is also used in MoRES model (Burkitov et al. [2016]).

3.4 Pressure & Extraction History Matching

History matching consists in adjusting the 3 parameters characterizing the reservoir to best fit the pressure measurements given the production flow rates. We minimize the misfit between the modeled and the measured pressure at the boreholes, consisting of 1186 static (bottom well pressure is assumed to differ from wellhead pressure only due to the hydrostatic effect due to the weight of the fluid column) measurements between 1957 and 2017 across 29 different locations. We use a simple three-dimensional grid search of space of model parameters. The minimum, maximum and separation between grid points are given in Table 1 leading to a total of 12400 simulations of pressure depletion models. The fit is quantified using a simple root mean square error (RMSE). The reported pressure measurements don't have uncertainties associated to them so we give equal weight to all the measurements. The best fitting model yields pressure histories that are remarkably consistent the observations (Figure 2). Figure 3 shows the residuals from the best fitting VFE model and from MoReS as a function of time. The best fitting VFE model corresponds to a permeability of $3.1 \pm 0.68 \times 10^{-13} m^{-2}$ a porosity of $18.5 \pm 6.5\%$, and a gas saturation of $27 \pm 2.4\%$. These values are consistent with average permeability ($3.55 \times 10^{-13} m^{-2}$) and porosity (17%) reported by (Burkitov et al. [2016]). Based on the figures presented in this report, the gas saturation should be in the range between 0.26 and 0.35, so pour estimate seems conistent as well. The best VFE model yields a RMSE of 5.5 MPa compared to 3.5 MPa for MoReS (Figure 3). This is a remarkably good fit given that the VFE model has only 3 adjustable parameters compared to 96 for MoReS. The distribution of residuals in space show larger misfits, a larger difference between the VFE and MoReS model prediction in the southwestern area of the reservoir which might in fact be poorly connected to the main reservoir (3). We also note a North-South gradient in the comparison between the MoReS and the VFE model, which is probably due to the fact that our model ignores the interaction with the aquifer at the northern edge of the reservoir. Another most obvious difference is the drift of the VFE residuals to larger values starting in the 1990s. No such drift is visible in the MoReS residuals, probably due to the account for the presumed intrusion of the aquifer bounding the reservoir to the North. The VFE could be tweaked to account for this effect by allowing for variations of the gas saturation. We didn't try to keep the model as simple as possible, and also because a more rigorous approach would consist is using a multiphase VFE model (Jenkins et al. [2019]). Altogether the best-fitting VFE model yields a pressure depletion history remarkably close to the pressure evolution predicted by MoReS. We estimate the uncertainties on the VFE model parameters using Chi-Square statistics. We note however that the residuals are not normally distributed Figure 3 and that our uncertainty quantification could be improved. We assume that the model is well-specified and that the residuals are dominated by model errors, in particular because of the assumption of homogeneous properties. We assume that measurements from one single well have a correlated model error and that measurements made at different wells are independent. We choose a confidence level or 95%. Given the number of model parameters, 3, and the number of wells, 29, the 95 % confidence domain on the model parameters is given by all the parameter sets yielding a RMSE of less than 6.191 MPa. The uncertainties on each model parameter is derived from the corresponding marginal distributions (1). The framework could allow implementation of a more sophisticated method of uncertainty quantification could be implemented that would allow estimating the complete probability distribution of model parameters based on a likelihood function accounting for a priori knowledge of model parameters and the fit to the observations.

3.5 Prediction of Pressure Evolution for Future Production Scenarios

Our VFE model can then be used to forecast the pressure evolution in time and space for various hypothetical production scenarios. The Shut-In scenario assumes a sudden arrest of production at the end of 2016. The 'Cold-Winter' production scenario uses temperature forecasts to determine how much Gas would be required in the case of cold winters starting from January 2017, and transitioning to complete shut-in of the reservoir by 2030 (Nederlandse Aardolie Maatschappij [2013]). We also simulated the pressure evolution for the Cold-Winter production scenario assuming pressure management. In this third scenario we consider that production is compensated by injection so that the net volume of fluid in the reservoir is kept constant from the beginning of 2017 on. We assumed gas extraction at the wells located in the southern portion of the gas field, where the reservoir is shallower, compensated by injection at the same rate at the wells located in the northern portion of the field (see locations of extracting and injecting wells in the inset of Figure 4). Although a simplistic representation the reservoir gas extraction distribution. We assumed that the gas is extracted from the shallower part We acknowledge that this simulation is not very realistic as the injected fluid is assumed to have the same properties as the extracted fluids since our VFE model considers only one phase. Using the history matched Vertical Flow Equilibrium model we can forecast the pressure depletion for each of these scenarios taking into account the uncertainties on the model parameters. To do so, for each scenario, we store the model predictions of all models within the 95% confidence domain derived from history matching. We use this model ensemble to forecast subsidence and seismicity om the next sections.

4 Geomechanical Modeling and Surface Subsidence

Surface subsidence over the Groningen gas field has been well documented with different geodetic and remote sensing techniques including optical levelling, persistent scatterer interferometric synthetic aperture radar (PS-InSAR) and continuous GPS (cGPS). (Smith et al. [2019]) combined all these data to describe the evolution of surface subsidence and the related reservoir compaction from the start of gas production until 2017.Here we show that the VFE model predicts a reservoir compaction consistent with the measured surface subsidence (Figure 5). For a given distribution of pressure depletion within the reservoir the surface displacement since the onset of production can be estimated assuming poroelastic compaction of the reservoir. Given the relatively shallow depth of the reservoir compared to its lateral extent, strain can be assumed uniaxial and vertical. The uniaxial compaction due to pressure depletion then only depend on the compressibility of the reservoir (Geertsma, J. [1973]) according to

$$\Delta h = C_m h \Delta P, \tag{13}$$

where Δh is the compaction of the reservoir, C_m the uniaxial compressibility, ΔP the pressure drop and h the reservoir thickness. The deforming reservoir might be represented as a series of point sources of strain (van Wees et al. [2019], Candela et al. [2019]). This approach is efficient as the Green Functions are analytical. It allows to calculate strain and stress changes in the 3-D volume and can feed a seismicity forecasting scheme easily. The method is however very sensitive to the distribution of the point sources representing the reservoir and to the distribution of the receiver points where stress changes are evaluated due to the stress singularity at the source location. Here the deforming reservoir is represented as a series of cuboidal volumes which are deforming poroelastically and assumed to be isotropic and homogeneous. It is an efficient way to represent, to the first order, spatial variations of the reservoir geometry, due in particular to the faults offsetting the reservoir. The displacement and stress Green's functions for polyhedral volumes are semi-analytical and can be obtained by integration of the point source solution (Geertsma, J. [1973]) over the volume of each cuboid (Kuvshinov [2008]). The distribution of uniaxial compressibility over the reservoir was estimated by (Smith et al. [2019]) based on the pressure depletion predicted by MoReS, the reservoir thickness, and the reservoir compaction derived from the linear inversion of the surface displacements measured from InSAR and GPS.

Figure 5 compares the time evolution of the spatial pattern of compaction predicted by our VFE model and MoReS with the compaction derived from the inversion of the geodetic and remote sensing measurements of surface subsidence (Smith et al. [2019]). It shows that both the VFE and MoReS predicts a compaction quite consistent with the measured surface subsidence. MoReS does however better at fitting the spatial distribution of compaction. In fact, the VFE model fits the time evolution of the compaction derived from the surface displacements better than MoReS. The quality of the fit obtained with the VFE model is remarkable as the compressibility distribution was optimised to fit MoReS. The surface measurement of displacement could therefore be included in the dataset used for reservoir history matching (van Oeveren et al. [2017]) and our framework would allow to introduce spatial variations of reservoir properties to improve the fit to both the pressure measurements and the surface subsidence. This could help refine the spatial distribution of the reservoir characteristics, including its geometry. This approach could be interesting to constrain reservoirs less well known than Groningen where injection or production would produced a measurable surface displacement signal. In any case, this comparison suggests that the strain, and the stress changes predicted by the VFE and MoReS models are valid to first order.

5 Stress-based Seismicity Forecasting

We describe here how induced seismicity is predicted based on the temporal evolution of the fluid pressure distribution predicted by the reservoir model. Rock failure is commonly assessed using the Mohr-Coulomb failure criterion (Handin [1969]). A number of studies have demonstrated that this criterion applies effectively to assess earthquake triggering by stress changes (King et al. [1994]). According to this criterion failure occurs when the shear-stress τ exceeds the shear-strength of the material τ_f, represented by

$$\tau_f = \mu(\sigma_n - P) + C_0, \tag{14}$$

where τ_f is shear-stress, σ_n is the normal-stress (positive in compression), P is the pore pressure, μ is the internal friction and C_0 is the cohesive strength. If the material is not at failure the strength excess is $\tau_f - \tau$. Fluid pressure changes play an important role in preventing or promoting fault failure. Assuming the total stresses do not change, a greater pore pressure acts to lower the effective normal stress and promotes failure. By contrast, a pressure decrease should inhibit failure. It is therefore customary to assess jointly the effect of stress changes and pore pressure changes using the Coulomb stress change defined as

$$\Delta CFF = \Delta\tau + \mu(\Delta\sigma_m + \Delta P), \tag{15}$$

where ΔCFF is the change in Coulomb stress (the notation is customary and refers to the 'Coulomb Failure Function'; an alternative common notation is ΔCFS for 'Coulomb Failure Stress'), $\Delta\tau$ is the shear stress change, μ is the internal friction, $\Delta\sigma_m$ is the change in normal stress, and ΔP is the change in pore pressure.

Detailed studies of the seismicity show hypocenters within the reservoir (Dost et al. [2017], Willacy et al. [2019], Spetzler and Dost [2017]), or in the caprock (Smith et al. [2020]). We thus need to model the stress redistribution due to the reservoir compaction and pore pressure variations within and outside the reservoir with account for poroelastic effects (Wang [2018]). A number of previous studies have explored different approaches. (Bourne et al. [2018]) developed the Elastic Thin Sheet model (ETS), a semi-analytical reservoir depth integrated model. The ETS formulation approximates the reservoir deformation as a uniaxial vertical strain field, with zero horizontal strain. It does not describe the associated caprock deformation but allows estimating stress changes within the reservoir. It was designed to account for stress concentrations at the faults offsetting the reservoir. The faults characteristics are not explicitly represented but accounted for indirectly from the smoothed spatial gradient of the reservoir thickness. Another approach relies on the cuboids representation of the reservoir used to model surface subsidence. It can indeed be used to calculate stress changes within and outside the reservoir (Kuvshinov [2008], **?**). The knowledge of faults geometry can be accounted for via the cuboid mesh. The two approaches were implemented in our framework and compared in the previous study based on MoReS (**?**). They make equivalent predictions so, for the purpose of this study, we use only the ETS model which is computationally more effective.

The next element needed to forecast seismicity needs to relate stress changes to seismicity. The time of onset of seismic slip on a particular fault will depend on the initial stress and on the rheological law relating stress to fault slip. Methods based on the rate and state friction law determined in laboratory studies (Dieterich [1994]) have shown success, in particular in applications to induced seismicity at Groningen (Candela et al. [2019], Richter et al. [2020]). The original formulation of (Dieterich [1994]) assumes that all faults are initially 'above steady state' meaning that they are assumed to have been on their way to failure from the start of perturbation of the stress field when gas production started. A significant improvement was obtained by relaxing this hypothesis (Heimisson et al. [2021]). This new formulation assumes that the faults were initially in a relaxed state, which is a reasonable finding in the stable tectonic context of the Groningen gas field. The consequence is that the formulation introduces a stress threshold needed to be exceeded for earthquake nucleation. This threshold is equivalent to the stress change, the 'initial strength excess', needed to reach the condition for failure in the case of simple static Coulomb failure model. With the introduction of this threshold it turns out that the duration of the nucleation process, the time needed to reach failure, is greatly reduced so that assuming instantaneous failure provides a good approximation of the seismicity rate (smith2021). The computational cost of the model is then significantly reduced. We therefore adopt here the simple assumption of instantaneous nucleation once a the stress change equates an initial strength excess which is treated as a stochastic quantity. The stochastic representations provides a way to account for stress heterogeneity and the diversity of fault orientations. These assumptions lead to a model of (Bourne and Oates [2017]) which assumes that the seismicity only reflects the tail of the failure probability function (failure of the faults with the smallest strength excess). However, it is possible that the seismicity may have transitioned to a more steady regime in which case the representation of only the tail of the distribution might be inadequate. We therefore adopt a modified version of the model. For each fault the distribution of strength excess depends on the probability distributions describing its orientation, stress and strength. Heterogeneities of stress resulting from variations of elastic properties of lithological origin can result in a Gaussian distribution of Coulomb stress changes (Langenbruch and Shapiro [2014]). If we assume that the initial Coulomb stress values on different fault patches are independent and identically distributed random values, the probability of failure of a fault at a location with a maximum Coulomb stress changes ΔC is derived from integration of the Gaussian function yielding (Smith2021),

$$P_f = \frac{1}{2}\left(1 + \mathrm{erf}\left(\frac{\Delta C - \theta_1}{\theta_2\sqrt{2}}\right)\right), \tag{16}$$

where θ_1, θ_2 represent the mean and standard deviation of the Gaussian distribution, representing the fault strength distribution. While the extreme value theory implies an exponential rise of seismicity for a constant stress rate (Bourne and Oates [2017]), the seismicity rate will gradually evolve to a regime where the seismicity rate will be proportional to the stress rate as the stress increases to a value of the order of the mean initial strength excess (θ_1). If the faults that have already ruptured are allowed to re-rupture and if the Coulomb stress has increased to a value significantly larger than the typical stress drop during an earthquake, the distribution of strength excess will become uniform (constant between 0 and the co-seismic stress drop); the seismicity rate would then remain proportional to the stress rate. This is the steady regime expected an active tectonic setting for instantaneous nucleation (Ader et al. [2014]). The formulation allows in principle the system to move out of the initial exponential rise of seismicity. A third parameter, where θ_0, is needed to represent the density of nucleation points per unit area. This parameters depends primarily on the detection threshold of the seismicity catalog used for model calibration. Hypocentral depths are not accounted for since, with the ETS formulation, earthquakes are assumed to occur within or at the boundary of the reservoir.

For consistency with the study of (Heimisson et al. [2021]), we quantify the misfit between the predicted and observed seismicity using a Gaussian log-likelihood function

$$\log(p(m \mid R^o)) = -\frac{1}{2}\sum_{i=1990}^{i=2016}\left(R_i^o - \int_\Sigma R(m,i,x,y)dxdy\right)^2, \tag{17}$$

where $R(m,i)$ is the model predicted rate density in year i, where m is the vector of model parameters. R_i^o is the observed rate in year i. Integration in Easting, x, and Northing y, is carried over the area Σ corresponding to the outline of the reservoir in mapview. During the training we sample the PDF (Equation 17) using an Metropolis-Hastings sampler. After sufficient number of samples, hindcasts are obtained by selecting 1000 random samples of $m = m_1, m_2, \ldots$ at random and computing $R^p(m,t)$ for $t > y_e + 1$. For calibration of the model, we use the catalogue of (Dost et al. [2017]) which reports earthquake locations since 1990, with a completeness of $M_{LN} > 1.5$ since 1993. The model parameters and their uncertainties derived using the best fitting (MAP) history matched VFE model are listed in Table 2. We also list the mean and the range of model parameters obtained from the ensemble of models within the 95% confidence domain determined during the history matching procedure. The model parameters derived when using MoReS as input to the stress calculation are listed in Table 3. They are close those obatined with VFE models.

Not surprisingly, the spatial and temporal variations of seismicity rate predicted with either the VFE models or the MoReS model are very similar and quite consistent with the observations (Figure 6). One noticeable difference is that the VFE models predicts more seismicity than MoReS in the southwestern area of the reservoir. This is due to the fact that the VFE models predict a smaller pore pressure drop in that area than MoReS. By contrast the VFE model predicts a lesser seismicity rate than MoReS in the central part of the reservoir. Both models are consistent to first order with the observed distribution of earthquakes. Figure 6d shows the mean expected annual seismicity rate (blue line), and the range of expected seismicity rate for the ensemble of VFE models within the 95 % confidence domain derived from history matching. The two models predict a seismicity rate consistent with the observations over the validation period. A slightly better validation fit is actually obtained with the VFE model. It should be noticed that the plot doesn't account for the variability of seismicity rate expected from the stochastic nature of seismicity. here is therefore more variability in the observed rate. This term could be included assuming a non-homogeneous Poisson process and some model of aftershock statistics such as ETAS (Ogata [1998]). It is not included here as it would obscure the contribution of the uncertainties on reservoir model parameters. Figure 6 also shows the expected maximum magnitude based on the VFE and MoReS models. This calculation assumes that the frequency-magnitude distribution of earthquakes follow the Gutenberg-Richter law for a b-value of 1. For simplicity we didn't include any consideration for the uncertainty and possible temporal variations of the b-value (Bourne and Oates [2020]).

Once the history matched seismicity production values are determined, we can forecast the earthquake rate for the different hypothetical production scenarios described above. Figure 7 shows the seismicity forecast for the cold winter scenario, the shut-in scenario and the cold winter scenario with pressure management. The shut-in scenario leads to the most abrupt drop of seismicity. Seismicity doesn't completely shut down however because of pressure readjustment in the gas field after production is stopped. It should be noticed that the model doesn't account for the lag in the seismicity response that would result from the earthquake nucleation which is not instantaneous, as assumed in our model, but time dependent. Comparison with Figure 6 of Heimisson et al. (Heimisson et al. [2021]), which accounts for the effect of the nucleation process but assumes no further stress changes after shut-in, shows that the induced lag is in fact quite short. It is however probable that our model predicts a too abrupt drop of seismicity at the time of shut-in because this effect is neglected.

5.1 Conclusion

When combined with semi-analytical formulations to calculate poro-elastic stress changes and a simple model of earthquake nucleation, the Vertical Flow Equilibium assumption allows calculating reservoir fluid pressure, compaction, surface subsidence and induced seismicity at a low computational cost. The VFE assumption appears to be a valid approximation in the context of the Groningen gas field. It indeed leads to predictions of surface subsidence and seismicity consistent with observations and close to the predictions obtained based of the more sophisticated model, MoReS, which was developed by the operator. It thus provides a tool to assess the expected subsidence and seismicity response to production scenarios with account for uncertainties with bootstrapping or Monte-Carlo methods for example. In principle, our modeling framework could also be used to optimize pressure management. The location and the flow rates of the injection wells could for example be adjusted so that seismicity and subsidence would be minimized. A limitation of the model presented here is that it considers only one single fluid phase. In the context of Groningen, this is probably the reason for the drift in the residuals obtained from history matching with the VFE model. This issue does not appear with the MoReS model which allows groundwater intrusion at the northern boundary of the field. A multiphase VFE flow model could be implemented (Jenkins et al. [2019]) to alleviate that limitation. This would be beneficial also for the application of this framework to other applications where multiphase flow is required such as for CO_2 storage.

Acknowledgments

We are most gratelul to Ruby Fu and Mateo Acosta for discussions and suggestions. We gratefully acknowledge data from Nederlandse Aardoli Maatschappij (Jan Van Elk, Gini Ketellar and Dirk Doornhof), Shell Global Solutions (Stijn Bierman, Steve Oates, Rick Wentinck, Xander Campman, Alexander Droujinine and Chris Harris, and Koninkljjk Nederlands Meteorologisch Instituut (http://www.knmi.nl/)

Funding

This study was supported by the NSF/ IUCRC Geomechanics and Mitigation of Geohazards (National Science Foundation award #1822214). We acknowledge support from Shell Global Solutions.

Data Availability

The VFE code presented in this study can be found at the interactive Google Colab notebook `https://colab.research.google.com/drive/??`

Contributions

Hadrien Meyer: software development, manuscript and figures preparation. J.D. Smith: conceptualization, software development, manuscript and figures preparation. S.J.Bourne: conceptualization, manuscript editing. J.-P. Avouac: Supervision, Conceptualization and manuscript writing.

References

Thomas J Ader, Nadia Lapusta, Jean-Philippe Avouac, and Jean-Paul Ampuero. Response of rate-and-state seismogenic faults to harmonic shear-stress perturbations. *Geophysical Journal International*, 198(1):385–413, 2014.

M. S. Alnaes, J. Blechta, J. Hake, A. Johansson, A. Kehlet, B.and Logg, C. Richardson, J. Ring, M. E. Rognes, and Wells G. N. The FEniCS project version 1.5. *Archive of Numerical Software*, 3, 2015. doi: 10.11588/ans.2015.100.20553.

Daniel T. Birdsell, Satish Karra, and Harihar Rajaram. On the representation of the porosity-pressure relationship in general subsurface flow codes. 54(2):1382–1388, 2018. ISSN 00431397. doi: 10.1002/2017WR022001. URL `http://doi.wiley.com/10.1002/2017WR022001`.

S. J. Bourne and S. J. Oates. Extreme threshold failures within a heterogeneous elastic thin sheet and the spatial-temporal development of induced seismicity within the groningen gas field: Extreme failures and induced seismicity. 122(12):10,299–10,320, 2017. ISSN 21699313. doi: 10.1002/2017JB014356. URL `http://doi.wiley.com/10.1002/2017JB014356`.

S. J. Bourne and S. J. Oates. Stress-dependent magnitudes of induced earthquakes in the groningen gas field. *Journal of Geophysical Research: Solid Earth*, 125(11):e2020JB020013, 2020. doi: https://doi.org/10.1029/2020JB020013. URL `https://agupubs.onlinelibrary.wiley.com/doi/abs/10.1029/2020JB020013`. e2020JB020013 10.1029/2020JB020013.

S. J. Bourne, S. J. Oates, J. van Elk, and D. Doornhof. A seismological model for earthquakes induced by fluid extraction from a subsurface reservoir. *Journal of Geophysical Research: Solid Earth*, 119(12):8991–9015, 2014. doi: https://doi.org/10.1002/2014JB011663. URL `https://agupubs.onlinelibrary.wiley.com/doi/abs/10.1002/2014JB011663`.

S J Bourne, S J Oates, and J van Elk. The exponential rise of induced seismicity with increasing stress levels in the Groningen gas field and its implications for controlling seismic risk. *Geophysical Journal International*, 213(3):1693–1700, 03 2018. ISSN 0956-540X. doi: 10.1093/gji/ggy084. URL `https://doi.org/10.1093/gji/ggy084`.

L Buijze, PAJ Van den Bogert, BBT Wassing, and B Orlic. Nucleation and arrest of dynamic rupture induced by reservoir depletion. *Journal of Geophysical Research: Solid Earth*, 124(4): 3620–3645, 2019.

Loes Buijze, Peter AJ Van Den Bogert, Brecht BT Wassing, Bogdan Orlic, and Johan Ten Veen. Fault reactivation mechanisms and dynamic rupture modelling of depletion-induced seismic events in a rotliegend gas reservoir. *Netherlands Journal of Geosciences*, 96(5):s131–s148, 2017.

Ulan Burkitov, van Oeveren, Henk, and Valvatne, Per. Groningen field review 2015 subsurface dynamic modelling report. page 131, 2016. URL `https://www.lebonbon.fr/paris/loisirs/8-idees-de-balades-cools-a-paris/`.

H. Byrne, J. A. Silva, A. Plesch, R. Juanes, and J. H. Shaw. The groundbreaking experiment in earthquake control at rangely, colorado, revisited. *Geophysical Research Letters*, 47(11): e2020GL088257, 2020. doi: https://doi.org/10.1029/2020GL088257. URL `https://agupubs.onlinelibrary.wiley.com/doi/abs/10.1029/2020GL088257`. e2020GL088257 2020GL088257.

Thibault Candela, Sander Osinga, Jean-Paul Ampuero, Brecht Wassing, Maarten Pluymaekers, Peter A Fokker, Jan-Diederik van Wees, Hans A de Waal, and Annemarie G Muntendam-Bos. Depletion-induced seismicity at the groningen gas field: Coulomb rate-and-state models including differential compaction effect. *Journal of Geophysical Research: Solid Earth*, 124(7):7081–7104, 2019.

K.H. Coats, J.R. Dempsey, and J.H. Henderson. The use of vertical equilibrium in two-dimensional simulation of three-dimensional reservoir performance. 11(1):63–71, 1971. ISSN 0197-7520. doi: 10.2118/2797-PA. URL `http://www.onepetro.org/doi/10.2118/2797-PA`.

L.R. Cowton, J.A. Neufeld, N.J. White, M.J. Bickle, G.A. Williams, J.C. White, and R.A. Chadwick. Benchmarking of vertically-integrated CO2 flow simulations at the sleipner field, north sea. 491: 121–133, 2018. ISSN 0012821X. doi: 10.1016/j.epsl.2018.03.038. URL `https://linkinghub.elsevier.com/retrieve/pii/S0012821X18301687`.

H. Darcy. *Les fontaines publiques de la ville de Dijon: Exposition et application des principes à suivre et des formules à employer dans les questions de distribution d'eau : Ouvrage terminé par un appendice relatif aux fournitures d'eau de plusieurs villes, au filtrage des eaux et à la fabrication des tuyaux de fonte, de plomb, de tôle et de bitume.* V. Dalmont, 1856. URL `https://books.google.fr/books?id=42EUAAAAQAAJ`.

Jan de Jager and Clemens Visser. Geology of the groningen field – an overview. 96(5):s3–s15, 2017. ISSN 0016-7746, 1573-9708. doi: 10.1017/njg.2017.22. URL `https://www.cambridge.org/core/product/identifier/S0016774617000221/type/journal_article`.

G De Marsily. Quantitative hydrogeology. 1 1986. URL `https://www.osti.gov/biblio/6784827`.

David Dempsey and Jenny Suckale. Physics-based forecasting of induced seismicity at groningen gas field, the netherlands. *Geophysical Research Letters*, 44(15):7773–7782, 2017.

James Dieterich. A constitutive law for rate of earthquake production and its application to earthquake clustering. *Journal of Geophysical Research: Solid Earth*, 99(B2):2601–2618, 1994. doi: https://doi.org/10.1029/93JB02581.

Bernard Dost, Elmer Ruigrok, and Jesper Spetzler. Development of seismicity and probabilistic hazard assessment for the groningen gas field. *Netherlands Journal of Geosciences*, 96(5):s235–s245, 2017.

Geertsma, J. Land subsidence above compacting oil and gas reservoirs. page 11, 1973.

John Handin. On the coulomb-mohr failure criterion. *Journal of Geophysical Research*, 74(22): 5343–5348, 1969.

Elias Rafn Heimisson, Jonathan D Smith, Jean-Philippe Avouac, and Stephen Bourne. Coulomb threshold rate-and-state model for fault reactivation: Application to induced seismicity at Groningen. 2021. doi: https://doi.org/10.31223/X5489T.

Luke T. Jenkins, Martino Foschi, and Christopher W. MacMinn. Impact of pressure dissipation on fluid injection into layered aquifers. *Journal of Fluid Mechanics*, 877:214–238, aug 2019. doi: 10.1017/jfm.2019.593. URL `https://doi.org/10.1017%2Fjfm.2019.593`.

Birendra Jha and Ruben Juanes. Coupled multiphase flow and poromechanics: A computational model of pore pressure effects on fault slip and earthquake triggering. *Water Resources Research*, 50(5):3776–3808, 2014. doi: https://doi.org/10.1002/2013WR015175. URL `https://agupubs.onlinelibrary.wiley.com/doi/abs/10.1002/2013WR015175`.

R. Juanes, B. Jha, B. H. Hager, J. H. Shaw, A. Plesch, L. Astiz, J. H. Dieterich, and C. Frohlich. Were the may 2012 emilia-romagna earthquakes induced? a coupled flow-geomechanics modeling assessment. *Geophysical Research Letters*, 43(13):6891–6897, 2016. doi: https://doi.org/10.1002/2016GL069284. URL `https://agupubs.onlinelibrary.wiley.com/doi/abs/10.1002/2016GL069284`.

Geoffrey CP King, Ross S Stein, and Jian Lin. Static stress changes and the triggering of earthquakes. *Bulletin of the Seismological Society of America*, 84(3):935–953, 1994.

Kayla A. Kroll, Thomas A. Buscheck, Joshua A. White, and Keith B. Richards-Dinger. Testing the efficacy of active pressure management as a tool to mitigate induced seismicity. *International Journal of Greenhouse Gas Control*, 94:102894, 2020. ISSN 1750-5836. doi: https://doi.org/10.1016/j.ijggc.2019.102894. URL `https://www.sciencedirect.com/science/article/pii/S1750583618307242`.

Boris N Kuvshinov. Elastic and piezoelectric fields due to polyhedral inclusions. *International Journal of Solids and Structures*, 45(5):1352–1384, 2008.

C. Langenbruch and S. A. Shapiro. Gutenberg-richter relation originates from coulomb stress fluctuations caused by elastic rock heterogeneity. *Journal of Geophysical Research: Solid Earth*, 119(2):1220–1234, 2014. doi: https://doi.org/10.1002/2013JB010282. URL `https://agupubs.onlinelibrary.wiley.com/doi/abs/10.1002/2013JB010282`.

Anthony L. Lee, Mario H. Gonzalez, and Bertram E. Eakin. The Viscosity of Natural Gases. *Journal of Petroleum Technology*, 18(08):997–1000, 08 1966. ISSN 0149-2136. doi: 10.2118/1340-PA. URL `https://doi.org/10.2118/1340-PA`.

Nederlandse Aardolie Maatschappij. A technical addendum to the winningsplan groningen 2013 subsidence, induced earthquakes and seismic hazard analysis in the groningen field. *NAM, Assen*, 2013.

Yosihiko Ogata. Space-time point-process models for earthquake occurrences. *Annals of the Institute of Statistical Mathematics*, 50(2):379–402, 1998. doi: 10.1023/A:1003403601725.

Gudrun Richter, Hainzl Sebastian, Dahm Torsten, and Zöller Gert. Stress-based, statistical modeling of the induced seismicity at the groningen gas field, the netherlands. *Environmental Earth Sciences*, 79(11), 2020.

Jonny Rutqvist, Antonio P Rinaldi, Frederic Cappa, Pierre Jeanne, Alberto Mazzoldi, Luca Urpi, Yves Guglielmi, and Victor Vilarrasa. Fault activation and induced seismicity in geological carbon storage–lessons learned from recent modeling studies. *Journal of Rock Mechanics and Geotechnical Engineering*, 8(6):789–804, 2016.

Jonathan D. Smith, Jean-Philippe Avouac, Robert S. White, Alex Copley, Adriano Gualandi, and Stephen Bourne. Reconciling the long-term relationship between reservoir pore pressure depletion and compaction in the groningen region. page 2018JB016801, 2019. ISSN 2169-9313, 2169-9356. doi: 10.1029/2018JB016801. URL `https://onlinelibrary.wiley.com/doi/abs/10.1029/2018JB016801`.

Jonathan D. Smith, and Stephen J. Bourne Elias R. Heimisson, and Jean-Philippe Avouac. Stress-based forecasting of induced seismicity with instantaneous earthquake failure functions: Applications to the groningen gas reservoir. 2020.

Jesper Spetzler and Bernard Dost. Hypocentre estimation of induced earthquakes in groningen. *Geophysical Journal International*, 209(1):453–465, 2017.

A. J. Stauble and G. Milius. Geology of groningen gas field, netherlands. 1970.

Rob M.H.E. van Eijs and Onno van der Wal. Field-wide reservoir compressibility estimation through inversion of subsidence data above the groningen gas field. 96(5):s117–s129, 2017. ISSN 0016-7746, 1573-9708. doi: 10.1017/njg.2017.30. URL `https://www.cambridge.org/core/product/identifier/S0016774617000300/type/journal_article`.

Hendrik van Oeveren, Per Valvatne, Leendert Geurtsen, and Jan van Elk. History match of the groningen field dynamic reservoir model to subsidence data and conventional subsurface data. *Netherlands Journal of Geosciences*, 96(5):s47–s54, 2017. doi: 10.1017/njg.2017.26.

Jan-Diederik van Wees, Maarten Pluymaekers, Sander Osinga, Peter Fokker, Karin Van Thienen-Visser, Bogdan Orlic, Brecht Wassing, Dries Hegen, and Thibault Candela. 3-d mechanical analysis of complex reservoirs: a novel mesh-free approach. *Geophysical Journal International*, 219(2):1118–1130, 2019.

D. W. Vasco, R C Bissell, B. Bohloli, T. M. Daley, A. Ferretti, W. Foxall, B. P. Goertz-Allmann, V. Korneev, J P Morris, V Oye, A. L. Ramirez, A. P. Rinaldi, A. Rucci, J. Rutqvist, J. White, and R. Zhang. Monitoring and modeling caprock integrity at the in salah carbon dioxide storage site, algeria. *Geophysical Monograph Series*, 238, 11 2018. doi: 10.1002/9781119118657.

H Wang. Introduction to poroelasticity. 2018.

Chris Willacy, Ewoud van Dedem, Sara Minisini, Junlun Li, Jan-Willem Blokland, Indrajit Das, and Alexander Droujinine. Full-waveform event location and moment tensor inversion for induced seismicity. *Geophysics*, 84(2):KS39–KS57, 2019.

Shenglai Yang. *Fundamentals of petrophysics*. Springer Berlin Heidelberg, 2016. ISBN 978-3-662-53527-1.

Y C Yortsos. A theoretical analysis of vertical flow equilibrium. page 13, 1991.

Guang Zhai and Manoochehr Shirzaei. Fluid injection and time-dependent seismic hazard in the barnett shale, texas. *Geophysical Research Letters*, 45(10):4743–4753, 2018. doi: https://doi.org/10.1029/2018GL077696. URL https://agupubs.onlinelibrary.wiley.com/doi/abs/10.1029/2018GL077696.

Guang Zhai, Manoochehr Shirzaei, Michael Manga, and Xiaowei Chen. Pore-pressure diffusion, enhanced by poroelastic stresses, controls induced seismicity in oklahoma. *Proceedings of the National Academy of Sciences*, 116(33):16228–16233, 2019. doi: 10.1073/pnas.1819225116. URL https://www.pnas.org/doi/abs/10.1073/pnas.1819225116.

	Parameter Search			Optimised Value <95% confidence	
Parameter	Minimum	Maximum	Separation	MAP Value	Standard Deviation
Permeability (m^2)	1×10^{-13}	4.0×10^{-13}	1×10^{-14}	3.1×10^{-13}	6.78×10^{-14}
Porosity	0.1	0.2	0.005	0.185	0.0165
Gas Saturation	0.24	0.35	0.005	0.27	0.0268

Table 1: Parameter space used for running forward simulations of the reservoir pressure depletion

	Mean			Standard Deviation		
	θ_0	θ_1	θ_2	θ_0	θ_1	θ_2
unit	m^{-2}	MPa	MPa	m^{-2}	MPa	MPa
MAP Reservoir Pressure	0.291	0.075	-0.355	0.0211	0.0070	0.3118
Ensemble (95% confidence domain)	0.334	0.086	0.279	0.0468	0.0116	0.5400

Table 2: Mean and standard deviation of the parameters of the Gaussian stress threshold model used to relate stress changes to seismicity for the best fitting (MAP) VFE model and across all the pressure history match models within the 95% confidence domain.

	Mean			Standard Deviation		
	θ_0	θ_1	θ_2	θ_0	θ_1	θ_2
unit	m^{-2}	MPa	MPa	m^{-2}	MPa	MPa
MAP Reservoir Pressure	0.342	0.076	1.584	0.0097	0.0025	0.1755

Table 3: Mean and Standard deviation of the parameters of the Gaussian stress threshold model used to relate stress changes to seismicity for MoReS.

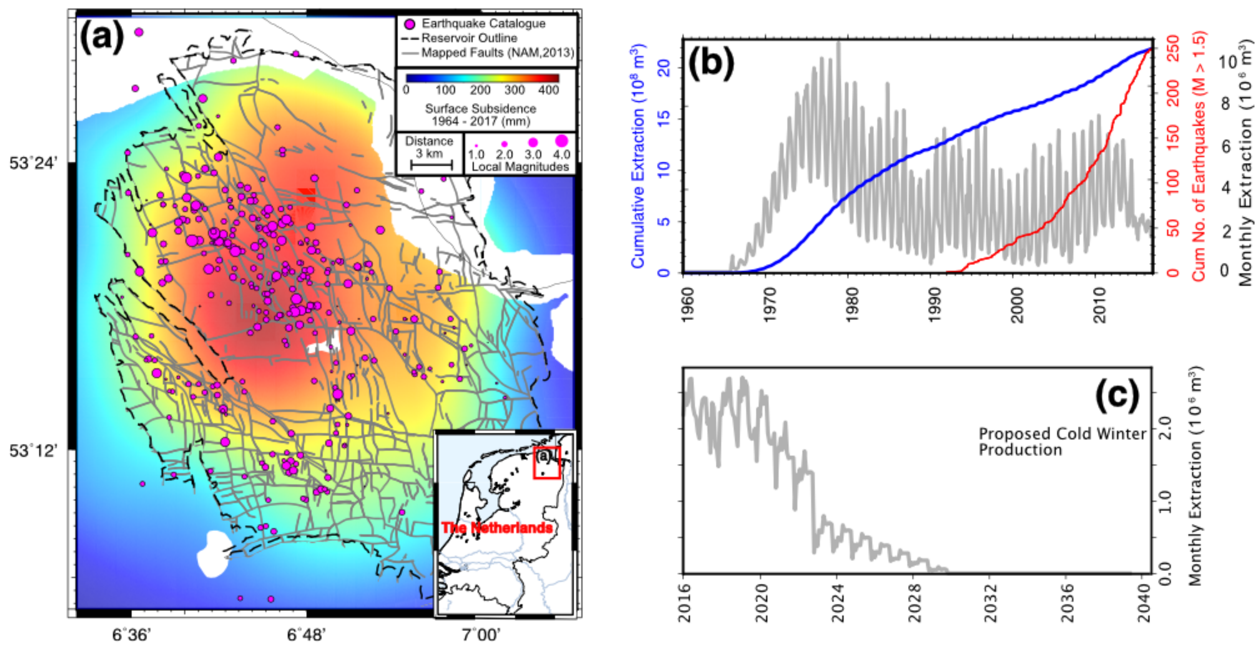

Figure 1: (a) Cumulated surface subsidence (Smith et al. [2019]) and seismicity between 1964 and 2017 (pink circles) (ref). The largest event reached ML = 3:6. Black dashed line shows the ouline of the gas reservoir. Grey lines show the faults affecting the reservoir (ref). (b) Cumulated gas production and cumulated number of earthquakes since the onset of gas production in 1959. (c) Planned production for the 'Cold Winter' scenario from the end of 2016 to 2030 (ref).

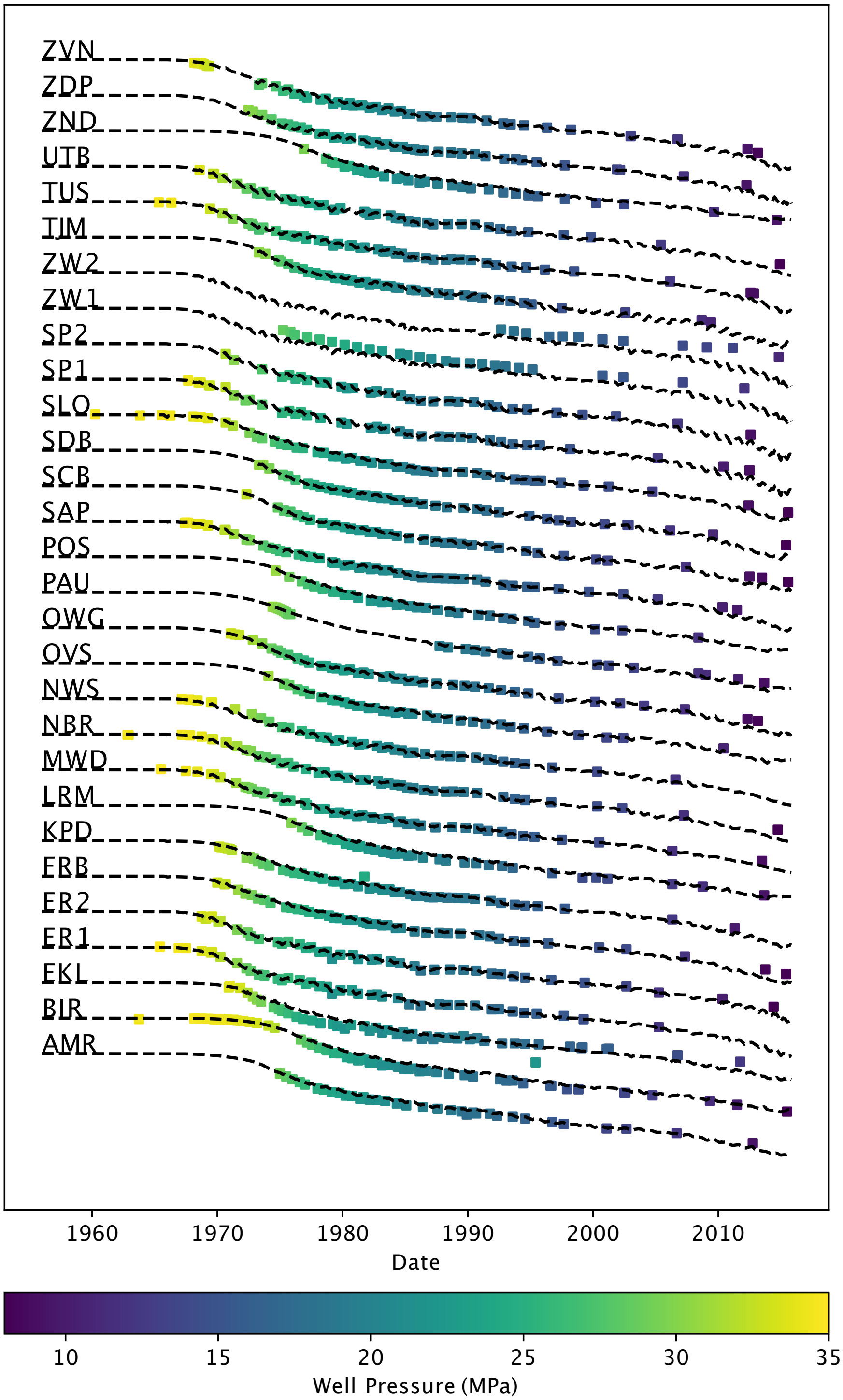

Figure 2: Comparison of measured well pressure with prediction from our history matched VFE model at all 29 wells.

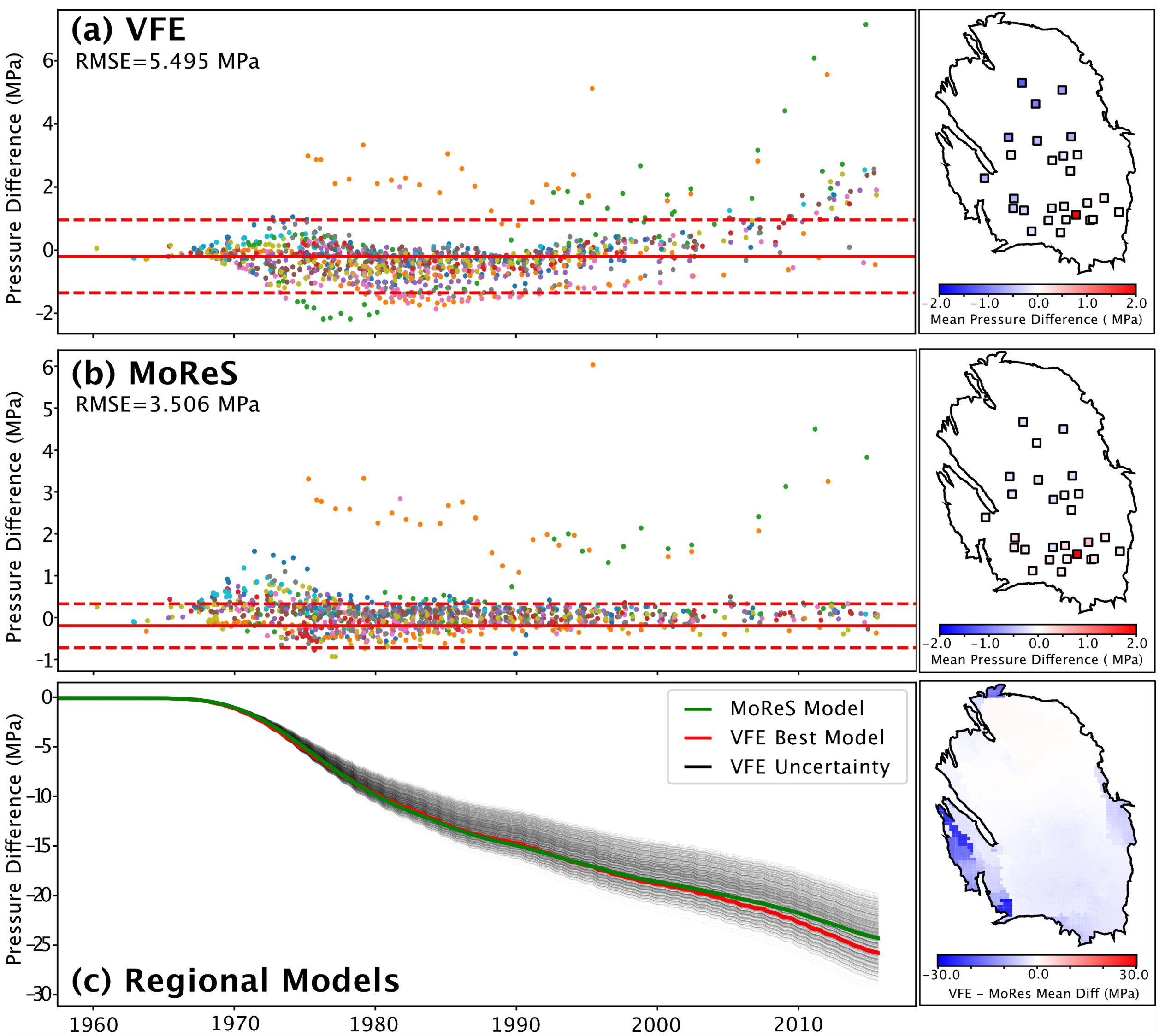

Figure 3: (a) Comparison of the reservoir pressure predicted by the history matched Vertical Flow Equilibrium (VFE) model and MoReS in time (left panel) and space (right panel). The red and green lines show the mean reservoir pressure predicted by the VFE and the MoReS models. Gray lines present the realizations of all the pressure depletion models with darker colors representing lower misfits. (b) Temporal (left panel) and spatial (right) distribution of misfits from the history matching of the VFE model. The red line shows the RMSE and the dashed lines encompass 88% of the residuals. (c) same as (b) for the MoReS model

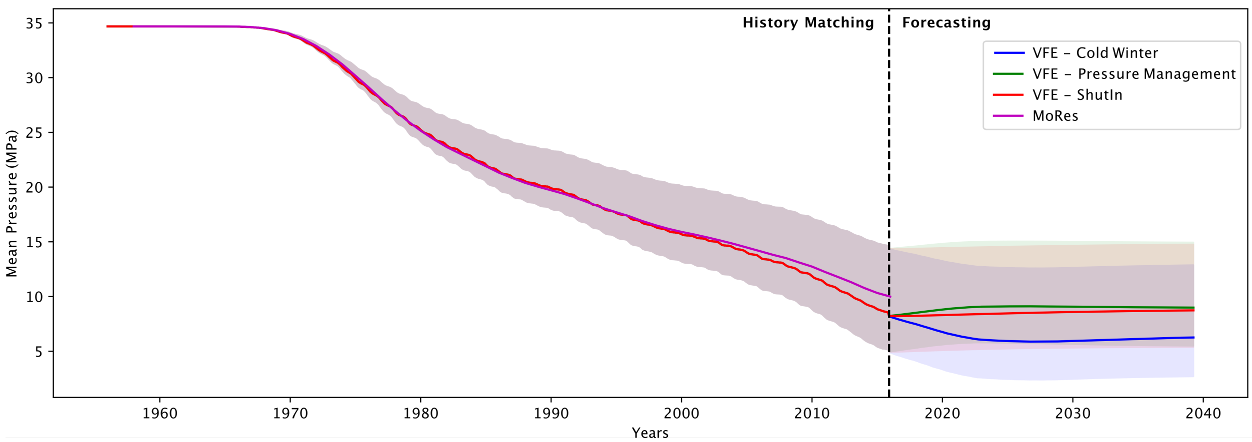

Figure 4: Predicted mean pressure evolution withe VFE model for the Shut-In scenario, the Cold-Winter production scenario and the Cold-Winter production with pressure management scenario. Inset shows the distribution of extraction and injection wells in the pressure management scenario. The lines and shaded areas show the prediction from the best VFE fitting model obtained from history matching and the associated 88% confidence interval assuming Shut-in (red), Cold-Winter (blue) and the Cold-Winter with pressure management (green) scenarios. The blue line and blue shading show the Cold-Winter prediction from the best fitting VFE model obtained from history matching and the associated 88% confidence interval. Blue and Blue region representing the vertical flow equilibrium model for Cold-Winter scenario with the solid line representing the optimal history matched scenario and bounding region emcompassing 88% of the measurements. The purple line shows the mean reservoir pressure from MoReS. The vertical dashed line marks the transition from history matching to forecasting in 2016.

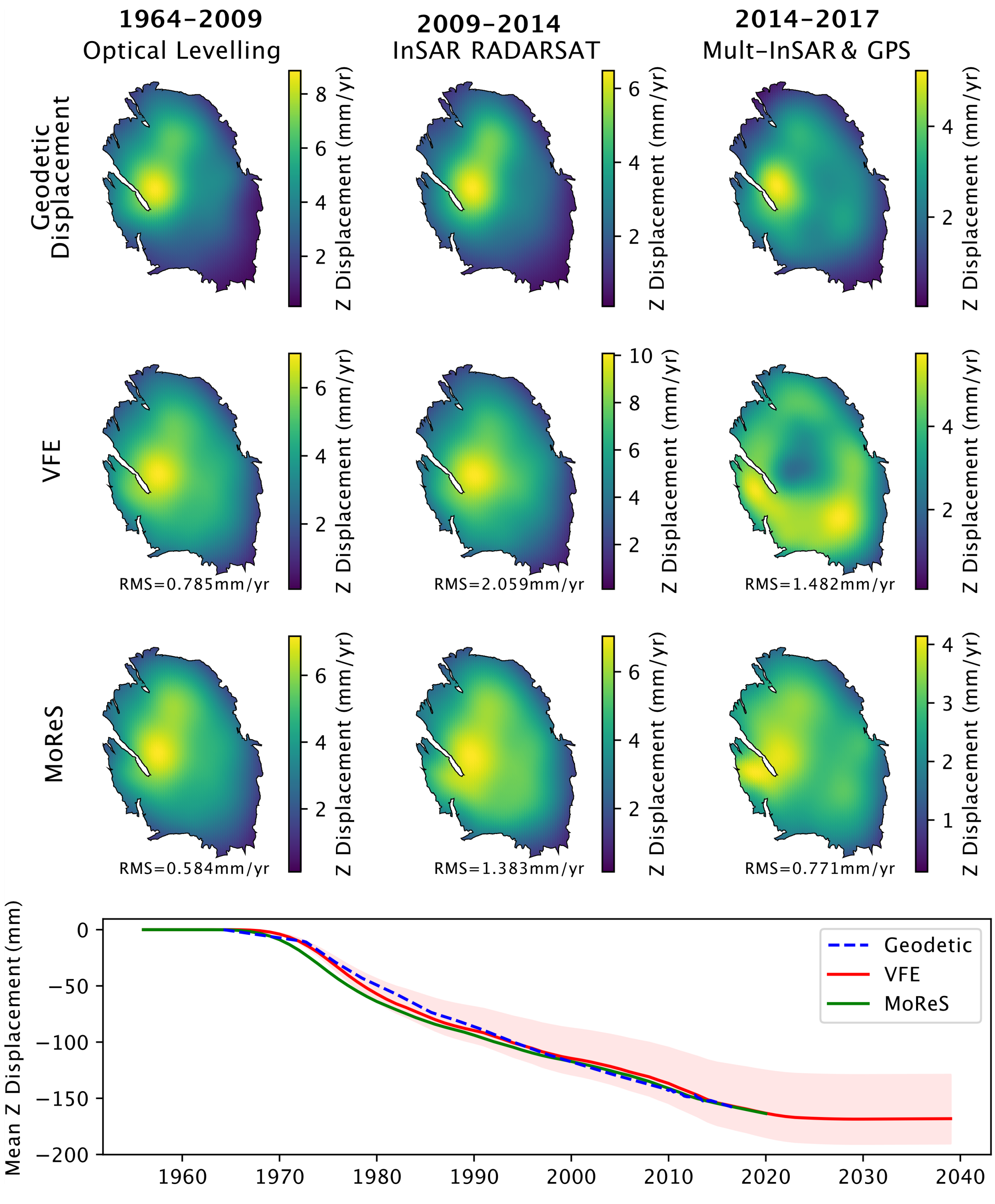

Figure 5: Comparison between the reservoir compaction derived from the inversion of the geodetic and inSAR measurements of surface displacement Smith et al. [2019] (1st row) with the compaction predicted based on the pressure distribution calculed with the VFE (2d row) and MoReS models (3d row) for different periods (columns). The root mean square (RMS) difference between the compaction derived from geodesy and from the reservoir models are reported on the panels. The bottom panel show the time evolution of the mean subsidence derived from the geodetic measurements and predicted by the VFE and MoReS models.

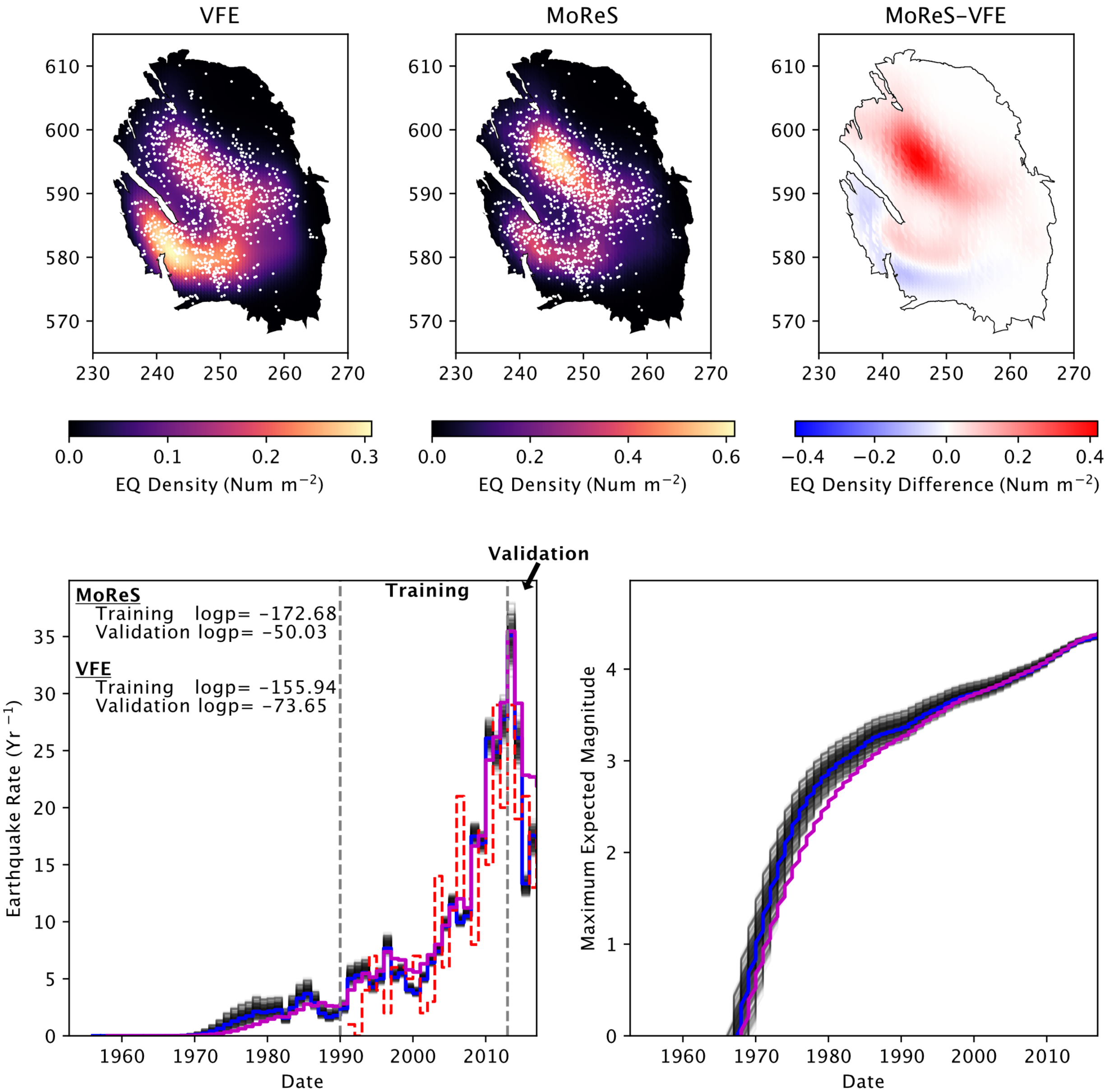

Figure 6: Spatial and temporal variations of seismicity rate predicted with our framework until 2016. Stress changes induced by poroelastic deformation of the reservoir were calculated either with MoReS or with our VFE models. (a) Observed seismicity (white dots) and density of earthquakes (color shading) predicted with the best fitting history matched VFE model. (b) Observed seismicity (white dots) and density of earthquakes (color shading) predicted with MoReS. (c) Expected annual seismicity rate for the best fitting history matched VFE model (blue line) and MoReS (purple line). Grey lines: range of expected seismicity rate for the ensemble of VFE models within the 95 % confidence domain derived from history matching. (d) Expected maximum magnitude predicted by tMoReS (purple line) and the VFE models (blue line for MAP model grey lines for 95 % confidence domain)

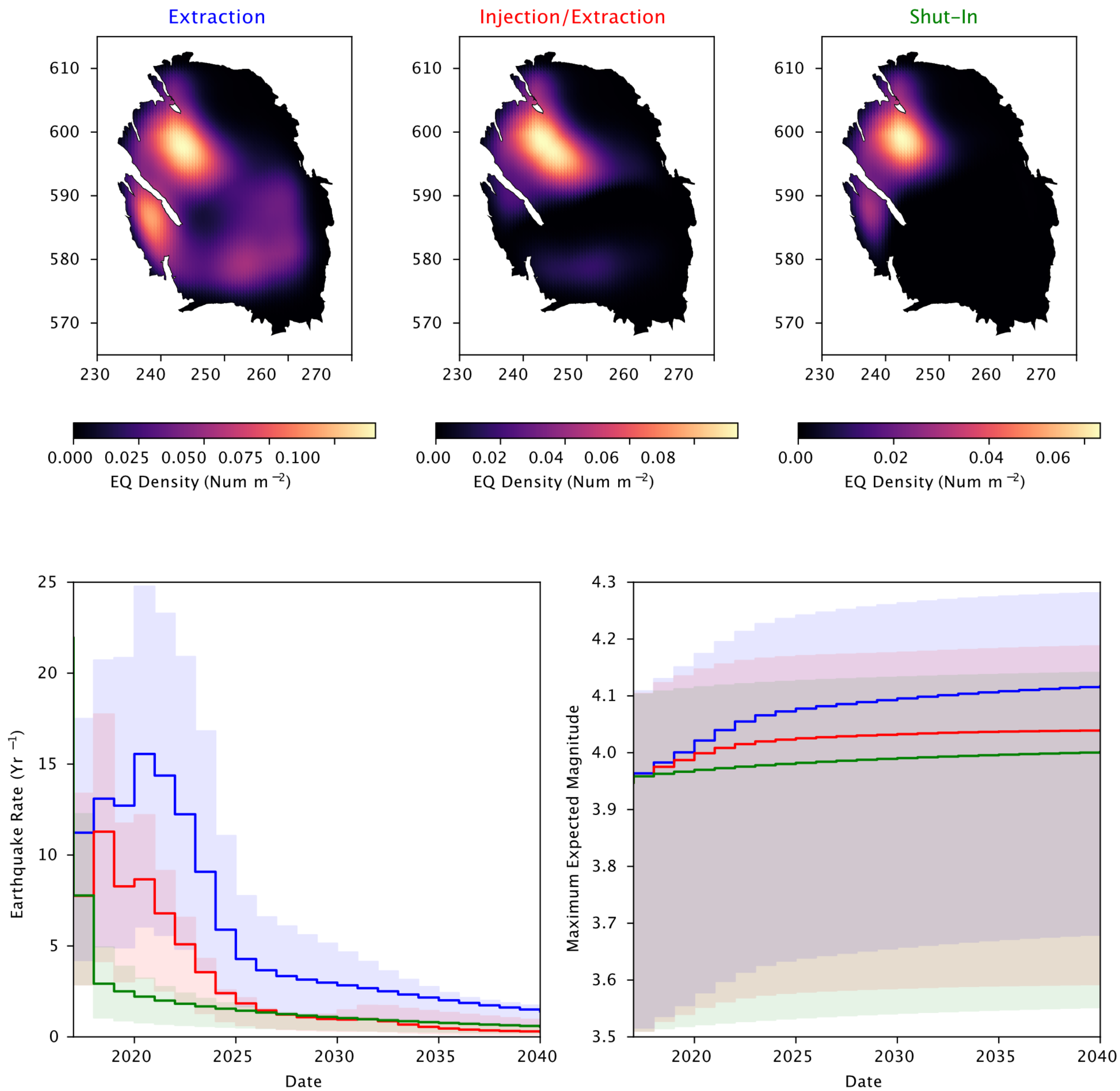

Figure 7: Predicted spatial distribution of seismicity from 2016 to 2030 using the MAP VFE model for the shut-in scenario (a), the cold winter scenario (b), and the cold winter scenario with pressure management (c). Temporal evolution of annual seismicity rate (d) and expected maximum magnitude (e) for the three scenarios. Shaded areas show the range of model predictions from the ensemble of VFE reservoir model within the 95% confidence domain. The expected maximum magnitude is calculated assuming a b-value of 1.